Published in IET Microwaves, Antennas & Propagation
Received on 19th December 2007
Revised on 30th July 2008
doi: 10.1049/iet-map:20070333

In Special Issue on Asia Pacific Microwave Conference 2007

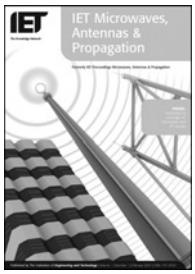

ISSN 1751-8725

Investigation of non-specular scattering by comparing directional channel characteristics from microcell measurement and simulation

N. Lertsirisopon[1] *G.S. Ching*[1] *M. Ghoraishi*[1] *J.-I. Takada*[1] *I. Ida*[2] *Y. Oishi*[2]

[1]*Department of International Development Engineering, Tokyo Institute of Technology, Tokyo, Japan*
[2]*Fujitsu Ltd., Tokyo, 105-7123, Japan*
E-mail: joy@ap.ide.titech.ac.jp

Abstract: Channel characteristics from microcell measurement and simulation are compared. In microcell environment, the dominant propagation mechanisms are not only from reflections and diffractions from buildings but can also come from non-specular scatterings. Propagation prediction tools such as ray-tracing algorithms which calculate only reflections and diffractions are hence not enough to completely predict the channel. To address this issue, an implementation called polygon meshed physical optics (polygon meshed PO) is used. Polygon meshed PO approximates the traditional PO by dividing the scatterer surface into triangular meshes to reduce the surface integral (for calculating the scattering field) into summation of mesh areas. This makes it flexible even for irregularly shaped objects. As PO utilises the whole illuminated scatterer surface to calculate the scattering field, it is not limited to specular directions and can be used to compute the contribution of non-specular scattering. To know the actual propagation channel, wideband measurement was performed inside a university campus. With antenna arrays on both the transmit and receive sides, wideband double-directional channel characteristics such as azimuth-delay power spectrum can be obtained after applying the conventional beamforming. Comparison of measurement and simulation results reveals that small metallic objects cause non-specular scattering and affect the propagation channel. These objects can be predicted by the proposed polygon meshed PO in cooperation with ray tracing.

1 Introduction

In mobile communication systems, multiple input multiple-output (MIMO) systems with antenna arrays both at the mobile station (MS) and base station (BS) have recently emerged as a key technology to increase the capacity and reliability of the systems [1, 2]. The performance of MIMO systems depends much on the directional and delay characteristics of the channel, and models of wireless propagation channel should include the directions of arrival (DoA), directions of departure (DoD) and time delay of the multipath components. Therefore to reflect the wideband double-directional structure of the radio channel in a considered propagation environment, realistic channel models [3, 4] are required instead of the conventional channel models which consider only delay characteristics.

On the other hand, ray-tracing algorithms are popular approaches for propagation prediction and modelling since the directional and delay characteristics of the channel are implied in each ray. It is a common knowledge that ray-tracing algorithms can predict elementary propagation mechanisms due to specular reflections from wall surfaces and diffraction from building edges [5, 6]. Since the dominant propagation mechanisms in macrocells are from wall reflections, building corner and roof-edge diffractions [7, 8], this might be applicable. But in smaller cells or microcells, the non-specular scattering from some small

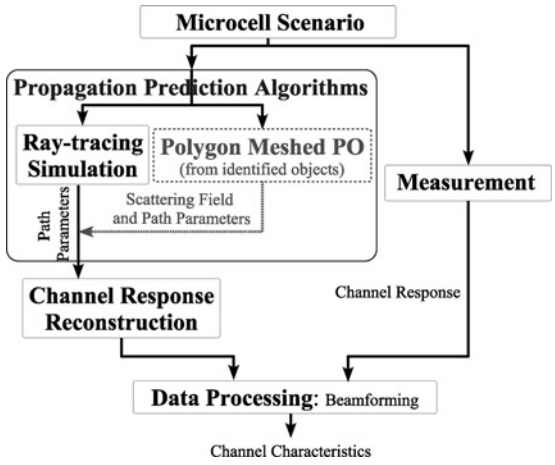

Figure 1 *Outline of this approach taken to investigate non-specular scattering*

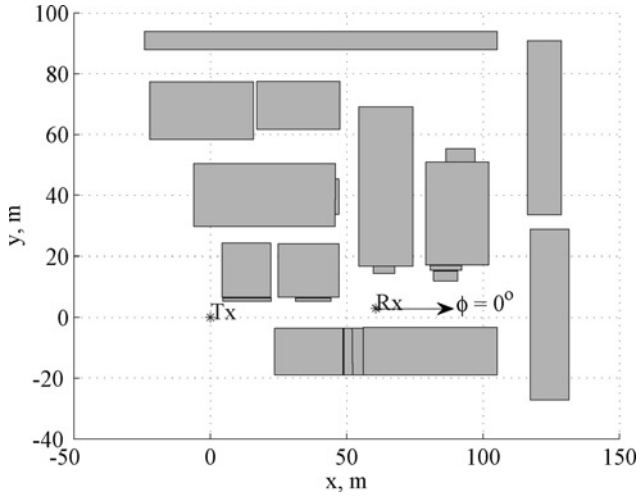

Figure 2 *Measurement scenario*

objects other than buildings can have significant contribution comparable to the dominant propagation mechanisms such as specular reflection and diffraction. However, this existing non-specular scattering [9, 10] is not yet included in ray-tracing algorithms.

To study the impact of those scattering objects, geometrical optics (GO) and geometrical theory of diffraction which are currently used to simulate the propagation channel for mobile communications cannot be applicable since all elementary waves of an incident plane wave are assumed reflected at the same ideally smooth planar boundary. Instead, we are going to use physical optics (PO) to simulate the scattering from small objects relative to the first Fresnel zone of the scattering paths. As PO [11] utilises the whole illuminated scatterer surface to calculate the scattering field, it is not limited to specular directions and can be used to compute the contribution of non-specular scattering. To simplify the calculation of the induced current and the scattering field, an implementation called polygon meshed PO is used. Polygon meshed PO approximates the traditional PO by dividing the scatterer surface into triangular meshes to reduce the surface integral (for calculating the scattering field) into summation of mesh areas. This makes it flexible even for irregularly shaped objects.

Therefore this paper proposes an alternative approach to predict the non-specular scattering from small shaped objects in cooperation with ray-tracing simulation in order to obtain a more accurate propagation prediction model for microcell scenarios. The outline of this approach is summarised as shown in Fig. 1.

2 Measurement scenario and equipment

The microcell measurement was carried out in O-okayama campus of Tokyo Institute of Technology [12]. In the following sections, we will describe the measurement scenario and employed equipment.

2.1 Scenario

In this measurement, the Tx antenna corresponds to the BS, whereas the Rx antenna corresponds to the MS. The BS antenna was fixed and mounted on a tripod with a height of 1.79 m from the ground, whereas the MS antenna with line-of-sight (LOS) to the BS was mounted on a cart with a height of 1.65 m. The 0° of the MS array antenna is pointing in the samedirection as the x-axis as illustrated in Fig. 2. The distance between BS and MS was 60 m.

Table 1 Specifications of measurement

Centre frequency	4.5 GHz
bandwidth	120 MHz
delay resolution	8.3 ns
excess delay	3.2 μs
frequency step	312.5 kHz
frequency samples	385
Tx power	40 dBm
Tx antenna	rectangular array, 2 × 4 dual polarised patch antenna
Tx antenna height	1.79 m
Rx antenna	cylindrical array, 2 × 24 dual polarised patch antenna
Rx antenna height	1.65 m

doi: 10.1049/iet-map:20070333

Table 2 Typical measured characteristics of patch antenna elements

	For BS antenna (HP port/VP port)	For MS antenna (HP port/VP port)
3 dB BW (horizontal plane)	89°/101°	86°/122°
3 dB BW (vertical plane)	94°/86°	89°/61°
antenna gain (main beam)	better than 5 dBi	better than 4 dBi
XPD (in both 3 dB BWs)	better than 11 dB	better than 10 dB

2.2 Channel sounding

The Medav RUSK Fujitsu channel sounder [13] was employed to accomplish the measurements and the related parameters can be found in Table 1.

The BS antenna is a 2×4 uniform rectangular antenna array of dual-polarised patch antenna elements, whereas the MS antenna array is a 2×24 stacked uniform circular antenna array with dual-polarised patches constituting 96 elements in total. The patch antenna elements on both BS and MS antenna array were characterised and summarised in Table 2. All values are based on measured antenna patterns when all patch antenna elements were attached. A periodic multicarrier frequency signal was utilised as the test signal at the centre frequency of 4.5 GHz allowing real time measurements of the channel response with a 120 MHz bandwidth resulting in a propagation delay resolution of 8.3 ns. To avoid delay ambiguities, the maximum measurable excess delay can be set according to the scenario. In our case, it was set to 3.2 μs (corresponding to a maximum measurable path length of $3.2\ \mu s \times 3 \times 10^8$ m/s = 960 m) which is sufficient for the given scenario. This corresponds to a frequency separation of (1/3.2 μs) 312.5 kHz. Reference clocks at both BS and MS ensure timing and switching frame synchronisation for the whole measurement durations. Fast switches were used in both Tx and Rx antenna arrays to switch the antenna ports to sample the received signal in the spatial domain. Accordingly, the total number of channels is 1536 including all combination of vertical polarisation (VP) and horizontal polarisation (HP).

3 Propagation prediction algorithms

The propagation prediction algorithms are separated based on specular and non-specular scattering. For specular scattering, the ray-tracing simulator is utilised, and the polygon meshed PO is utilised for the other case.

3.1 Ray-tracing simulator

The ray-tracing simulator called 'Raplab' [14] is used to predict detailed path parameters, that is, complex path gain, DoD and DoA in azimuth and elevation, and delay. This ray-tracing simulator consists of two major parts: a realistic three dimensional (3D) model of propagation environment and a model to calculate the multipath wave propagation between BS and MS. Buildings are generated according to their position and size similar to the measurement scenario (Fig. 2). Each building is modelled as a rectangular box by assuming the material parameters of concrete ($\varepsilon_r = 6.765$, $\mu_r = 1$, $\sigma = 0.0023$ s/m, thickness = 0.1 m).

A ray-optical wave propagation tool is used to calculate the channel between BS and MS, and distinguishes between different multipath components. Each path may consecutively experience different propagation phenomena. The propagation phenomena taken into account in the channel model are reflections, diffractions and combinations of multiple reflections and diffractions. The maximum reflection and diffraction used in this study are set to be 2 and 1, respectively. In order to trace rays from BS to MS, the method of image transmitters (image theory) [15] is implemented to find the ray paths and the angle is based on Snell's law of reflection. The formulation of reflected and diffracted rays is carried out based on GO and the uniform theory of diffraction (UTD) [16], respectively. The Fresnel reflection coefficients are used to model the reflections, whereas the coefficients for wedge diffraction are used for diffraction.

Ideal isotropic antennas are implemented to simulate the antenna independent channel. By tilting the BS and MS antenna, both VP and HP can be obtained. The output of Raplab generates a list of all propagation paths and its path parameters in each position.

3.2 PO approximation

PO is a type of high-frequency approximation method which is applicable to surfaces whose dimensions are large compared with the incident wavelength. In PO approximation [17], the induced electric current is approximated by applying the image theory at the scatterer which is assumed as a perfect electric conductor (PEC). This results in the tangential component of the magnetic field being double, while the normal component is cancelled. Then, the equivalent electric current $\boldsymbol{I}$ is approximated as $2\hat{n} \times \boldsymbol{H}^i$ on the illuminated part of the surface, whereas the equivalent magnetic current $\boldsymbol{M}$ is always 0, as the tangential electric field vanishes on the PEC surface [17]

$$\boldsymbol{I}^{\mathrm{PO}} = 2\hat{n} \times \boldsymbol{H}^i \qquad \text{for illuminated part}$$
$$\boldsymbol{M}^{\mathrm{PO}} = 0 \tag{1}$$

where $\hat{\boldsymbol{n}}$ is the normal vector from the surface. The electric vector potential ($\boldsymbol{A}$) and magnetic vector potential ($\boldsymbol{B}$) can be calculated from those induced current on the surfaces as

$$\boldsymbol{A} = \frac{1}{4\pi}\int_S \boldsymbol{I}^{\mathrm{PO}} \frac{\mathrm{e}^{-\mathrm{j}kr}}{r}\mathrm{d}S$$
$$\boldsymbol{B} = \frac{1}{4\pi}\int_S \boldsymbol{M}^{\mathrm{PO}} \frac{\mathrm{e}^{-\mathrm{j}kr}}{r}\mathrm{d}S = 0 \quad (2)$$

Therefore the scattering field at an observation point expressed in terms of the electric vector potential ($\boldsymbol{A}$) and the magnetic vector potential ($\boldsymbol{B}$) is simplified as

$$\boldsymbol{E}^s = -\mathrm{j}\omega\mu_0\boldsymbol{A} - \mathrm{j}\frac{\nabla\nabla\cdot\boldsymbol{A}}{\omega\varepsilon_0} - \nabla\times\boldsymbol{B}$$
$$= -\mathrm{j}\omega\mu_0\boldsymbol{A} - \mathrm{j}\frac{\nabla\nabla\cdot\boldsymbol{A}}{\omega\varepsilon_0} \quad (3)$$

where $\omega = 2\pi f$ and r is the distance between the integration point and the observer. ε_0 and μ_0 denote the permittivity and permeability of the free space, respectively, whereas k is the propagation constant in free space. Furthermore, the VP and HP of the incident field can also be considered in PO calculation.

(1) Polygon meshed PO: Polygon meshed PO is constructed by applying polygon meshes represented by several triangles. Since the scatterer is modelled by polygon meshes, the complex calculation of $\boldsymbol{A}$ can also be represented in the summation form of each polygon mesh instead of the surface integral in the case that each polygon mesh has a suitable size

$$\boldsymbol{A} = \frac{1}{4\pi}\int_S \boldsymbol{I}^{\mathrm{PO}} \frac{\mathrm{e}^{-\mathrm{j}kr}}{r}\mathrm{d}S \rightarrow \frac{1}{4\pi}\sum_{l=1}^{m} \boldsymbol{I}^{\mathrm{PO}} \frac{\mathrm{e}^{-\mathrm{j}kr}}{r}\Delta s_{\mathrm{m}} \quad (4)$$

where m is the number of polygon meshes and Δs_{m} is an area of each polygon mesh. To study about the convergence, a parameter called normalised polygon area is defined to determine the appropriate size of the polygon mesh as the following relationship

$$\text{Normalised polygon area} = \frac{\sum_{l=1}^{m}\Delta s_{\mathrm{m}}}{m\lambda^2} \quad (5)$$

The triangulation of a polygon is utilised since curved surfaces being subdivided into triangles can be handled efficiently. This algorithm is provided as an intrinsic function of MATLAB and utilises the constructive solid geometry model paradigm [18] to model the basic 2D geometrical objects and designs the meshed generation based on Delaunay triangulation [19]. For 3D geometrical objects, the height is mapped to the meshed 2D objects.

Furthermore, the parametric study and the analytical solutions were introduced in order to evaluate the performance of this approach as described in [20]. The verification was performed by comparing with the PO analytical model and the numerically accurate method of moments in the 2D geometrical case. The analytical solution of the perfectly conducting sphere was used in the 3D geometrical case. The parametric studies [21] showed that the normalised polygon area below 0.1 was sufficient for the scattering field to achieve convergence and made the performance of polygon meshed PO method similar to PO analytical one. Therefore the normalised polygon area below 0.1 was utilised in this simulation.

4 Channel reconstruction and data processing

From path parameters of ray-tracing results, the ray-based directional channel response can be modelled as [5]

$$\bar{\bar{H}}(f,\Omega^{\mathrm{BS}},\Omega^{\mathrm{MS}}) = \sum_{l=1}^{L}[\hat{\boldsymbol{\theta}}_l^{\mathrm{BS}}\ \hat{\boldsymbol{\phi}}_l^{\mathrm{BS}}]\begin{bmatrix}\gamma_{\mathrm{VV},l} & \gamma_{\mathrm{HV},l}\\ \gamma_{\mathrm{VH},l} & \gamma_{\mathrm{HH},l}\end{bmatrix}\begin{bmatrix}\hat{\boldsymbol{\theta}}_l^{\mathrm{MS}}\\ \hat{\boldsymbol{\phi}}_l^{\mathrm{MS}}\end{bmatrix}$$
$$\times\,\delta(\Omega^{\mathrm{BS}}-\Omega_l^{\mathrm{BS}})\cdot\delta(\Omega^{\mathrm{MS}}-\Omega_l^{\mathrm{MS}})\cdot\mathrm{e}^{(-\mathrm{j}2\pi f\tau_l)} \quad (6)$$

where L is the number of paths, $\hat{\boldsymbol{\theta}}_l^{\mathrm{BS}}$, $\hat{\boldsymbol{\theta}}_l^{\mathrm{MS}}$ the unit directional vectors of VP, $\hat{\boldsymbol{\phi}}_l^{\mathrm{BS}}$, $\hat{\boldsymbol{\phi}}_l^{\mathrm{MS}}$ the unit directional vectors of HP, γ the polarimetric complex path weights where the first and second subscripts correspond to MS and BS, respectively ($\gamma_{\mathrm{VV},l}$, $\gamma_{\mathrm{HH},l}$: co-polarisation components of VP and HP, and $\gamma_{\mathrm{HV},l}$, $\gamma_{\mathrm{VH},l}$: those of cross-polarisation components), $\Omega_l^{\mathrm{BS}} = (\boldsymbol{\theta}_l^{\mathrm{BS}},\boldsymbol{\phi}_l^{\mathrm{BS}})$, $\Omega_l^{\mathrm{MS}} = (\boldsymbol{\theta}_l^{\mathrm{MS}},\boldsymbol{\phi}_l^{\mathrm{MS}})$, $\boldsymbol{\theta}_l^{\mathrm{BS}}$, $\boldsymbol{\theta}_l^{\mathrm{MS}}$ the coelevation angles, $\boldsymbol{\phi}_l^{\mathrm{BS}}$, $\boldsymbol{\phi}_l^{\mathrm{MS}}$ the azimuth angles and τ_l the delay time.

The definitions of θ and ϕ components for BS and MS are illustrated in Fig. 3.

This model, however, does not include the effects of antenna structures. Note that the channel response from measurement results includes the complex vector directivity patterns of the antenna arrays. Therefore to reconstruct the channel response, $\boldsymbol{H}_{\mathrm{RT}}(f)$, the directional channel response from ray-tracing results should also include the

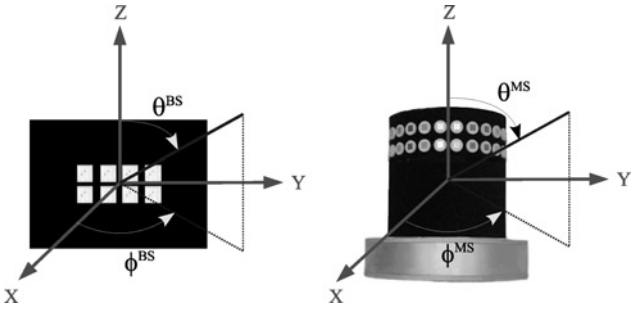

Figure 3 *Coordinate system at BS and MS, respectively*

doi: 10.1049/iet-map:20070333

array response as constructed by

$$\boldsymbol{H}_{\mathrm{RT}}(f) = \int\int_{\mathrm{BS}} \int\int_{\mathrm{MS}} \bar{\boldsymbol{b}}_{\mathrm{MS}}(\Omega^{\mathrm{MS}}) \cdot \bar{\bar{H}}(\boldsymbol{s}_{\mathbf{f}}) \cdot \bar{\boldsymbol{b}}^{\mathrm{H}}_{\mathrm{BS}}(\Omega^{\mathrm{BS}}) \mathrm{d}\Omega^{\mathrm{MS}} \mathrm{d}\Omega^{\mathrm{BS}} \quad (7)$$

where $\boldsymbol{s}_{\mathbf{f}} = [f, \Omega^{\mathrm{BS}}, \Omega^{\mathrm{MS}}]$, $\bar{\boldsymbol{b}}_{\mathrm{MS}}(\Omega^{\mathrm{MS}})$ and $\bar{\boldsymbol{b}}_{\mathrm{BS}}(\Omega^{\mathrm{BS}})$ are the MS and BS antenna array responses at the specified direction, respectively. $\bar{\boldsymbol{b}}^{\mathrm{H}}_{\mathrm{BS}}(\Omega^{\mathrm{BS}})$ denotes the hermetian transpose of $\bar{\boldsymbol{b}}_{\mathrm{BS}}(\Omega^{\mathrm{BS}})$. Note that ray tracing is conducted only at the centre frequency. To account for the frequency dependence of the phase delay in the exponential term of (6), the channel response is represented in vector form for all frequency samples as

$$\boldsymbol{b}_{\mathrm{RT}} = \begin{bmatrix} \mathrm{vec}\left(\boldsymbol{H}_{\mathrm{RT}} \frac{(f_{-(N_{\mathrm{f}}-1)})}{2}\right) \\ \vdots \\ \mathrm{vec}(\boldsymbol{H}_{\mathrm{RT}}(f_0)) \\ \vdots \\ \mathrm{vec}\left(\boldsymbol{H}_{\mathrm{RT}} \frac{(f_{(N_{\mathrm{f}}-1)})}{2}\right) \end{bmatrix} \quad (8)$$

where N_{f} is the number of frequency samples. Since the measured and simulated channel responses are available, the beamforming in the angular domain and matched filtering in the delay domain are conducted by using the weight vector $\boldsymbol{w}(\boldsymbol{s})$ as

$$\boldsymbol{w}(\boldsymbol{s}) = \boldsymbol{b}_{\mathrm{MS}}(\Omega^{\mathrm{MS}}) \otimes \boldsymbol{b}_{\mathrm{BS}}(\Omega^{\mathrm{BS}}) \otimes \boldsymbol{b}_{\mathrm{F}}(\tau) \quad (9)$$

and the resultant spectrum $P(\boldsymbol{s})$ is given as

$$P(\boldsymbol{s}) = \frac{|\boldsymbol{w}^{\mathrm{H}}(\boldsymbol{s})\boldsymbol{b}_{\mathrm{RT}}|^2}{\boldsymbol{w}^{\mathrm{H}}(\boldsymbol{s})\boldsymbol{w}(\boldsymbol{s})} \quad (10)$$

where $\boldsymbol{s} = [\tau, \Omega^{\mathrm{BS}}, \Omega^{\mathrm{MS}}]$ and $\boldsymbol{w}^{\mathrm{H}}$ denotes the hermetian transpose of $\boldsymbol{w}$. $\boldsymbol{b}_{\mathrm{F}}(\tau)$ is an impulse response.

Beamforming is applied in every 6° for the whole azimuth range (from 0° to 360°), and from 30° to 150° for the co-elevation due to antenna limitations.

5 Directional channel characteristics

Before proceeding, the authors would like to note that although the ray-tracing results can be compared directly with estimated ray parameters from the measurements results using a maximum likelihood estimator (RIMAX) [21], this comparison is not effective due to the different resolution limits for these two approaches. The angular and delay resolution of the former can be infinitesimally small, but that of the latter is physically limited by the bandwidth and size of the array antennas. Therefore the authors consider the limitation of the latter, and the beamforming/matched filtering output of the channel sounder and ray-tracing simulation are used for the comparison.

5.1 Azimuth-delay power spectrum

The measurement and the ray-tracing simulation results of the azimuth-delay power spectrum defined in (11) are shown in Fig. 4

$$P_{\mathrm{ADS}} = \frac{\sum_{\theta^{\mathrm{MS}}=1}^{N_{\theta^{\mathrm{MS}}}} \sum_{\theta^{\mathrm{BS}}=1}^{N_{\theta^{\mathrm{BS}}}} \sum_{\phi^{\mathrm{BS}}=1}^{N_{\phi^{\mathrm{BS}}}} (P_{V^{\mathrm{BS}}}(s) + P_{H^{\mathrm{BS}}}(s))}{N_{\theta^{\mathrm{MS}}} \cdot N_{\theta^{\mathrm{BS}}} \cdot N_{\phi^{\mathrm{BS}}}} \quad (11)$$

where $N_{\phi^{\mathrm{BS}}} = 61$, $N_{\theta^{\mathrm{BS}}} = N_{\theta^{\mathrm{MS}}} = 21$, $P_{V^{\mathrm{BS}}}$ and $P_{H^{\mathrm{BS}}}$ are the resultant spectrum of vertical and horizontal transmissions, respectively. From Fig. 4, the ray-tracing simulation can be seen to predict the arrival of strong

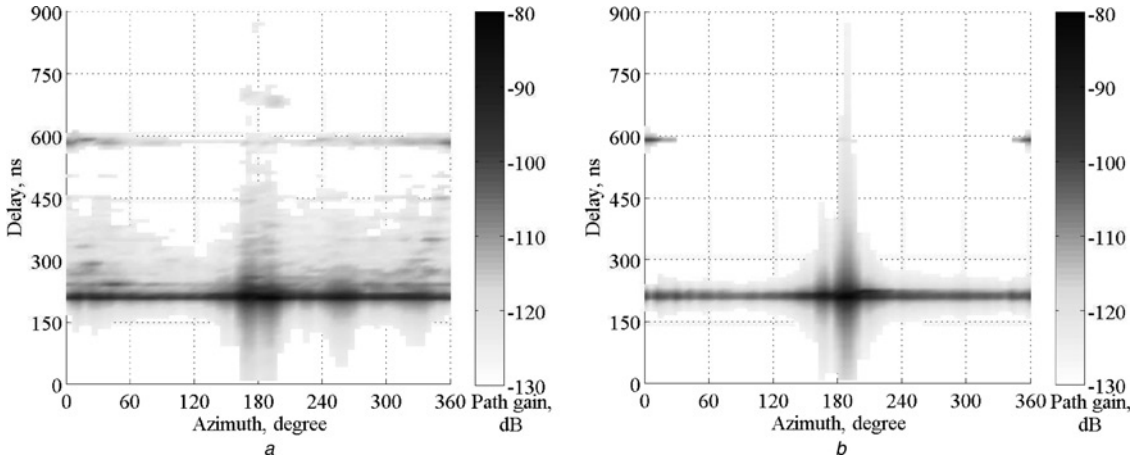

Figure 4 *Azimuth-delay spectrum:*

a Measurement
b Raplab

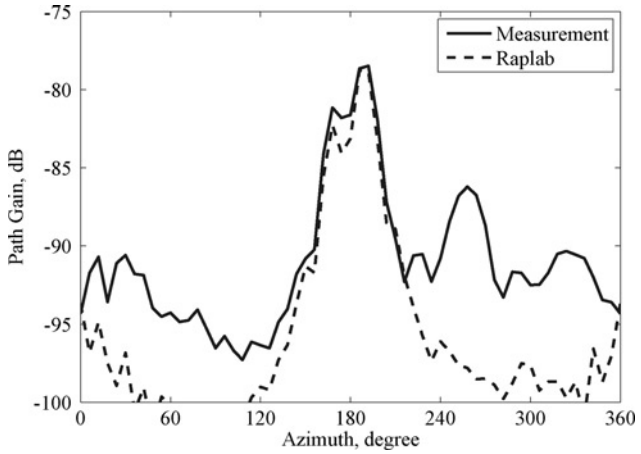

Figure 5 *Azimuth spectrum*

signals around 180°. A strong delayed path near 0° is also predicted corresponding to the building in front of MS.

(1) *Azimuth spectrum:* Azimuth spectrum can be obtained by summing up the power of azimuth-delay power spectrum with respect to the delay time. From Fig. 5, the arrival waves within the range from 138° to 216° are in agreement with respect to the shape of the spectrum. At 0°, some power is simulated by the ray-tracing algorithm corresponding to the building in front of MS. The remaining angles which do not match correspond to the right and left sides of the MS.

(2) *Delay spectrum:* Delay spectrum can be obtained by summing up the azimuth-delay power spectrum with respect to the azimuth angle. From Fig. 6, the ray-tracing simulation can predict accurately the two major peaks around 200 and 600 ns in the delay spectrum. For the 200 ns peak, it is composed of the LOS path and other paths close to it like reflections from the building walls in between BS and MS. The 600 ns peak corresponds to the previously mentioned building in front of MS.

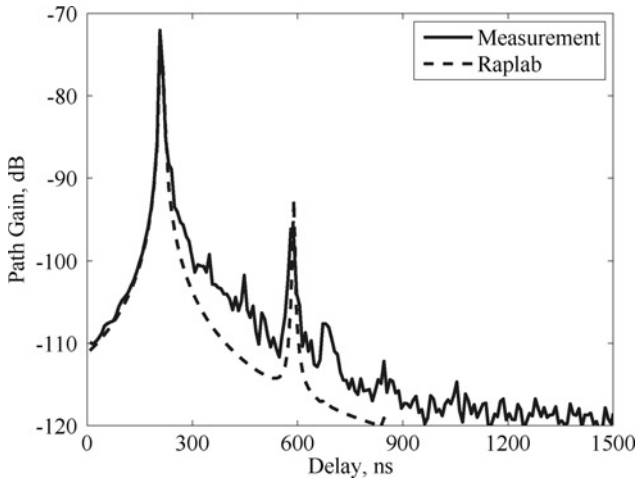

Figure 6 *Delay spectrum*

Figure 7 *Cluster in azimuth-delay power spectrum as seen from MS position*

5.2 Investigation of non-specular scattering

By aligning the pictures taken with fish-eye lens to the position of the receiver as shown in Fig. 7, the cluster within the second major peak of the azimuth spectrum given in Fig. 5 can be identified and it corresponds to the facilities constructed outside the building. As a supporting approach, the extracted paths estimated by RIMAX are manually inspected within the second major peak of the azimuth spectrum. Those extracted paths are in the azimuth range from 220° to 280° and delay from 201 to 205 ns as shown in Fig. 8 and are designated as a 'cluster'.

For the analysis, since the previous research [10] mentioned that the scattering from metallic objects such as lampposts and traffic lights can be comparable to the specular wall reflections and building edge diffractions therefore only metallic objects are analysed within this identified cluster and are shown in

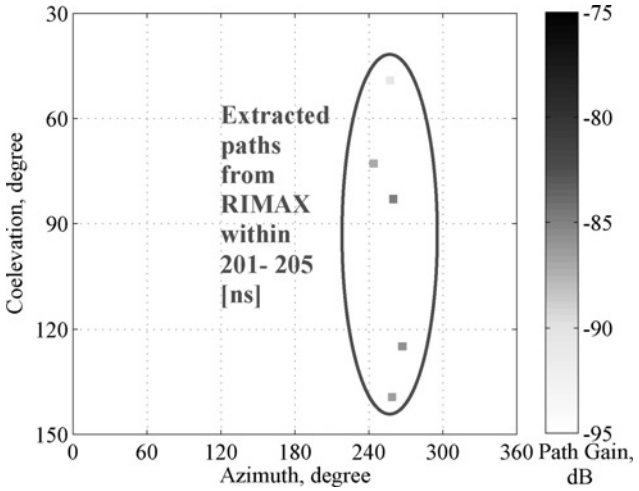

Figure 8 *Extracted paths from RIMAX*

doi: 10.1049/iet-map:20070333

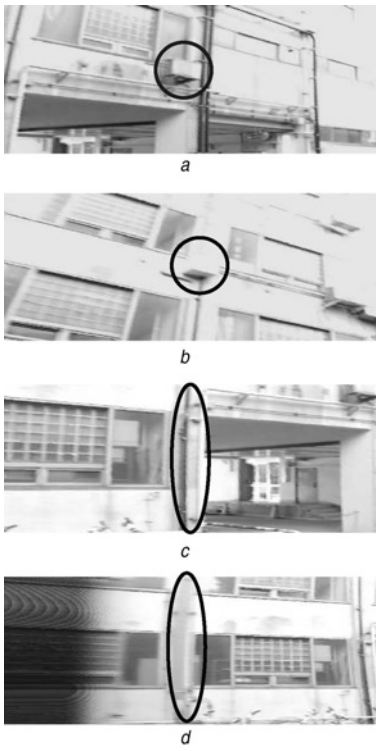

Figure 9 *Identified scatters within the cluster*

a Air conditioner at $\phi^{MS} \sim 222^{\circ}$
b Switch box at $\phi^{MS} \sim 239^{\circ}$
c 2 Metallic pipes at $\phi^{MS} \sim 239^{\circ}$
d Metallic pipe at $\phi^{MS} \sim 263^{\circ}$

Fig. 9. From these identified metallic objects, the polygon meshed PO is then utilised to model these objects and the scattering field at the receiver as well as the channel parameters such as delay, DoD and DoA are calculated. After incorporating the results of polygonmeshed PO with ray-tracing, the azimuth-delay power spectrum and azimuth spectrum are shown in Fig. 10.

From Fig. 10*a*, it is quite difficult to distinguish the difference from the azimuth-delay power spectrum of the previous ray-tracing simulation results in Fig. 10*b*. For Fig. 11, the second major peak can now be observed in the azimuth spectrum, although the result of this proposed approach still cannot match with the measurement result which may correspond to other scattering objects in the channel. However, this implies that those metallic objects do have effects in the propagation channel and can be predicted by polygon meshed PO.

Fig. 11 also shows the result of Raplab (designated as ObjectRaplab) by including the metallic objects into the environment model. Since Raplab still has some difficulties to handle curve surfaces in which the specular reflection always exists, even if those identified objects were included in the environment, the effect of those objects especially for the curve surfaces (pipes) cannot be observed in the azimuth spectrum. In general, the computation time for polygon meshed PO depends on the size of the objects since it will affect the number of polygons used. Moreover, the polygon meshed PO is not limited to metallic objects. It can also be used to handle tree trunks when it is modelled as a curve surface since Raplab handles curve surfaces with piecewise plane approximations. Although in this measurement, the location of the trees is not in the direction of the significant peaks, so we did not include it in the polygon meshed PO calculation. In other scenarios, tree trunks might have significant effect.

Finally, as the size of the microcell increases, the number of significant scatterers might also increase. For non-specular scattering, its effect maybe significant when the size of the object is smaller than the Fresnel zone, so that the GO formulation in Raplab is not applicable [22]. Therefore in this implementation, the size of the scatterer which is a bit smaller than the first Fresnel zone is the major target to be considered.

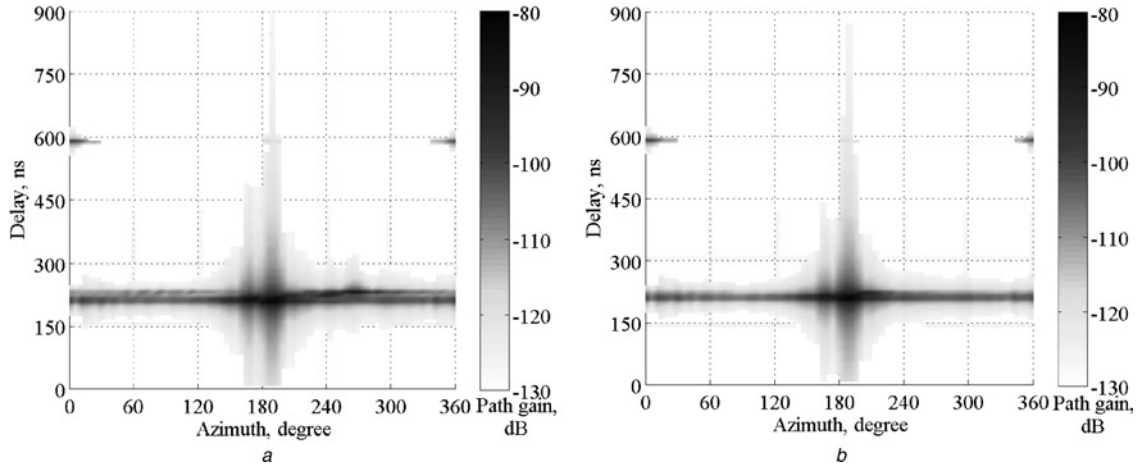

Figure 10 *Azimuth-delay spectrum:*

a Raplab + polygon meshed PO
b Raplab

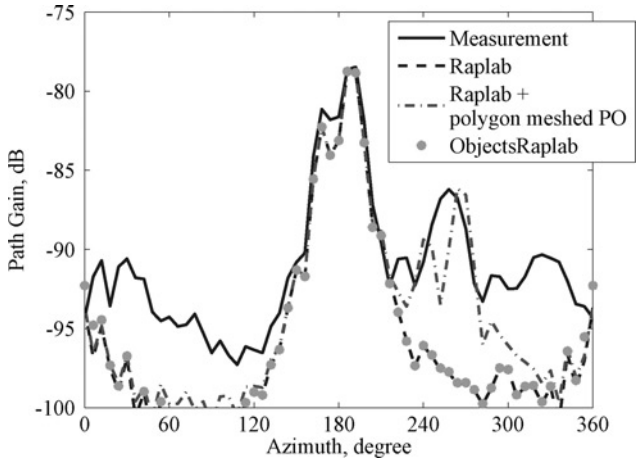

Figure 11 *Comparison of azimuth spectrum among four cases: measurement, Raplab, Raplab + polygon meshed PO, Raplab with additional objects (ObjectsRaplab)*

6 Conclusion

In this paper, a ray-tracing simulator was used to predict the path parameters of an LOS microcellular environment inside a university campus, and the results were applied to reconstruct the channel response. For data processing, the conventional beamforming is utilised to extract the wideband directional channel properties. These are then compared with channel properties from the measured results. The results show that the wideband directional channel properties from the ray-tracing result can predict the major peak appearing also in the measurement which corresponds to specular reflection and diffraction. To gain insight on the significant propagation mechanisms, the metallic scattering objects in the second major peak were identified by manual inspection with the aid of a camera with fish-eye lens.

The proposed approach called 'polygon meshed PO' is then utilised to model these scattering objects and to calculate the scattering field at the receiver as well as the channel parameters such as delay, DoD and DoA. After incorporating the results of polygon meshed PO with ray-tracing, the second major peak other than the LOS component can be observed which implied that those metallic objects have effect in the propagation channel in terms of non-specular scattering and can be predicted by polygon meshed PO. However, the procedure to consider the significant scattering objects would need to be developed in the future based on the results of this paper.

7 Acknowledgment

This research is supported by the National Institute of Information and Communications Technology of Japan (NICT). The authors would like to thank Dr. M. Landmann for his help in the field tests.

8 References

[1] 3GPP, TR 25.996: 'Spatial channel model for MIMO simulations', V6.1.0, September 2003

[2] MOLISCH A.F.: 'A generic model for MIMO wireless propagation channels in macrocells and microcells', *IEEE Trans. Signal Process*, 2004, **52**, pp. 61–71

[3] ASPLUND H., MOLISCH A., STEINBAUER M., MEHTA N.: 'Clustering of scatterers in mobile radio channels-evaluation and modeling in the COST259 directional channel model'. Proc. IEEE Int. Conf. Communication (ICC 2002), April 2002, vol. 2, pp. 901–905

[4] FUHL J., ROSSI J., BONEK E.: 'High-resolution 3D direction-of-arrival determination for urban mobile radio', *IEEE Trans. Antennas Propag.*, 1997, **45**, pp. 672–683

[5] ZHU H., TAKADA J., ARAKI K., KOBAYASHI T.: 'A ray-tracing-based characterization and verification of the spatio-temporal channel model for future wideband wireless systems', *IEICE Trans. Commun.*, 2001, **E84-B**, (3), pp. 644–652

[6] TAKADA J., FU J., ZHU H., KOBAYASHI T.: 'Spatio-temporal channel characterization in a suburban non line-of-sight microcellular environment', *IEEE J. Sel. Areas Commun.*, 2002, **20**, (3), pp. 532–578

[7] KALLIOLA K., LAITINEN H., VAINIKAINEN P., TOELTSCH M., LAURILA J., BONEK E.: '3-D double-directional radio channel characterization for urban macrocellular applications', *IEEE Trans. Antennas Propag.*, 2003, **51**, (11), pp. 3122–3233

[8] VUOKKO L., VAINIKAINEN P., TAKADA J.: 'Clusters extracted from measured propagation channels in macrocellular environments', *IEEE Trans. Antennas Propag.*, 2005, **53**, (12), pp. 4089–4098

[9] BUDIARTO H., HORIHATA K., HANEDA K., TAKADA J.: 'Experimental study of non-specular wave scattering from building surface roughness for the mobile propagation modeling', *IEICE Trans. Commun.*, 2004, **E87-B**, (4), pp. 958–966

[10] GHORAISHI M., TAKADA J., IMAI T.: 'Identification of scattering objects in the microcell urban mobile propagation channel', *IEEE Trans. Antenna Propag.*, 2006, **54**, (11), pp. 3473–3480

[11] TAKEUCHI T., SAKO M., YOSHIDA S.: 'Multipath delay prediction on a workstation for urban mobile radioenvironment'. Conf. Record of IEEE GLOBECOM, 1991, pp. 1308–1312

[12] LERTSIRISOPON N., CHING G.S., GHORAISHI M., TAKADA J., IDA I., OISHI Y.: 'Directional channel characteristics from microcell

doi: 10.1049/iet-map:20070333

measurement and simulation'. Asia Pacific Microwave Conf. (APMC 2007), December 2007

[13] LANDMANN M., SIVASONDHIVAT K., TAKADA J., IDA I., THOMÄ R.S.: 'Polarisation behaviour of discrete multipath and diffuse scattering in urban environments at 4.5 GHz', EURASIP, *J. Wirel. Commun. Netw.*, 2007, Article Id 57980

[14] Radio Propagation Laboratory (Raplab) accessed 2006, http://www4.kke.co.jp/raplab/

[15] VAUGHAN R., ANDERSEN J.B.: 'Channels, propagation and antennas for mobile communications' (The IEE, 2003)

[16] LUEBBERS R.J.: 'Finite conductivity uniform GTD versus knife-edge diffraction in prediction of propagation path loss', *IEEE Trans. Antennas Propag.*, 1984, **AP-32**, pp. 70–76

[17] ANDO M.: 'Physical optics', in YAMASHITA E. (ED.): 'Analysis methods for electromagnetic wave problems' (Artech House Inc., 1990, 2nd edn.), pp. 131–176

[18] BARBER C.B., DOBKIN D.P., HUHDANPAA H.T.: 'The quickhull algorithm for convex hulls', *ACM Trans. Math. Softw.*, 1996, **22**, (4), pp. 469–483

[19] KANAGANATHAN S., GOLDSTEIN N.B.: 'Comparison of four point adding algorithms for Delaunay type three dimensional mesh generators', *IEEE Trans. Magn.*, 1991, **27**, (3), pp. 3444–3451

[20] LERTSIRISOPON N., GHORAISHI M., CHING G.S., TAKADA J.: 'A study of scattering characteristics using PO polygon mesh'. Prog. Electromagn. Res. Symp. (PIERS 2006), August 2006

[21] THOMÄ R.S., HAMPICKE D., LANDMANN M., RICHTER A., SOMMERKORN G.: 'Measurement-based parametric channel modeling (MBPCM)', *Int. Conf. Electromagnetics in Advanced Application*, September 2003

[22] KISHIKI Y., TAKADA J.: 'Improvement of 3D ray tracing simulation in microcell environment by introducing the complex radar cross section'. 2008 Int. Symp. Antennas and Propagation (ISAP 2008), October 2008